

*What can the highest angular resolution bring to stellar astrophysics?*

*Editors : will be set by the publisher*

*EAS Publications Series, Vol. ?, 2024*

## STELLAR GRANULATION AND INTERFEROMETRY

A. Chiavassa<sup>1</sup> and L. Bigot<sup>1</sup>

**Abstract.** Stars are not smooth. Their photosphere is covered by a granulation pattern associated with the heat transport by convection. The convection-related surface structures have different size, depth, and temporal variations with respect to the stellar type. The related activity (in addition to other phenomena such as magnetic spots, rotation, dust, etc.) potentially causes bias in stellar parameters determination, radial velocity, chemical abundances determinations, and exoplanet transit detections.

The role of long-baseline interferometric observations in this astrophysical context is crucial to characterize the stellar surface dynamics and correct the potential biases. In this Chapter, we present how the granulation pattern is expected for different kind of stellar types ranging from main sequence to extremely evolved stars of different masses and how interferometric techniques help to study their photospheric dynamics.

### 1 Introduction

Stellar granulation was observed for the first time on the Sun by Herschel (1801), but it was Dawes (1864) who coined the term granules. Eventually, today modern telescopes provide direct observations (e.g., Carlsson *et al.*, 2004). The granulation pattern is associated with heat transport by convection, on horizontal scales of the order of a thousand kilometers (Nordlund *et al.*, 2009). On the other hand, convection is driven primarily by radiative cooling from a thin thermal boundary layer, the layer from which most photons can escape to space. The most prominent intensity variations on the solar surface, aside from sunspots and faculae, are granules i.e. the bright (hot) areas surrounded by dark (cooler) lanes that tile the stellar surface. The horizontal scale on which radiative cooling drives the convective motions is linked with the granulation diameter. The bright granules

---

<sup>1</sup> Laboratoire Lagrange, UMR 7293, CNRS, Observatoire de la Côte d’Azur, Université de Nice Sophia-Antipolis, Nice, France

are the locations of upflowing hot plasma, while the dark intergranular lanes are the locations of downflowing cool plasma (Nordlund *et al.*, 1990).

Stellar granulation manifests either on resolved observables (e.g., Sun images) or unresolved photospheric spectral line in terms of widths, shapes, and strengths. In particular, the best observational evidence comes from unresolved spectral lines because they combine, in their shapes, important properties such as velocity amplitudes (heavily affecting the line width) and velocity-intensity correlations (Nordlund *et al.*, 2009). Similarly, correlation of velocity and temperature cause characteristic asymmetries of spectral lines as well as net blueshifts (Dravins, 1987; Gray, 2005).

Stellar granulation potentially cause bias in stellar parameters, radial velocity, chemical abundances determinations, and exoplanet transit detections. For this purpose, large efforts have been made in recent decades to use theoretical modelling of stellar atmospheres to solve multidimensional radiative hydrodynamic equations in which convection emerges naturally. These simulations take surface inhomogeneities into account (e.g., granulation pattern) and velocity fields and are used to predict reliable observables. They cover a substantial portion of the Hertzsprung-Russell diagram (Magic *et al.*, 2013; Ludwig *et al.*, 2009), including the evolutionary phases from the main sequence over the turnoff up to the red-giant branch for low-mass stars. These simulations of stellar atmospheres are essential for much of contemporary astronomy.

## 2 Stellar atmosphere, a pathway to multi-dimensional simulations

The primary source of information for stellar objects is the light they emit, which carries information about the physical conditions at its origin. However, in order to interpret the information correctly, one first needs either theoretical or semi-empirical models of the atmospheric layers at the surface of stars from where the stellar radiation escapes. Many of the observable phenomena occurring on the surface of the stars are intimately linked to convection. Moreover, the atmospheric temperature stratification in the optically thin region, where the emerging flux form, is also affected by the interaction between radiative and convective energy transport. To account for all these aspects, it is important to use realistic 3D radiative hydrodynamical (RHD) simulations of stellar convection (Nordlund *et al.* 1998; Freytag *et al.* 2012; Ludwig *et al.* 2004; Vögler *et al.*, 2004).

RHD simulations numerically solves the time-dependent equations for conservation of mass, momentum, and energy coupled to a realistic treatment of the radiative transfer. The simulation domains are of two kinds: (i) *box-in-a-star* simulations (Fig. 1, right panel; computational time ranging from few days to few weeks depending on the stellar type) cover only a small section of the surface layers of the deep convection zone (typically ten pressure scale heights vertically), and the numerical box includes about  $\sim 10$  convective cells, which are large enough so that the cells are not constrained by the horizontal (cyclic) boundaries. (ii) *star-in-a-box* simulations (Fig. 1, left panel; computational time of few months) cover the whole convective envelope of the star and have been used to model evolved

cool stars like Red Supergiant stars, RSGs (Freytag *et al.*, 2012; Chiavassa *et al.*, 2011b) and Asymptotic Giant Branch stars, AGBs (Freytag *et al.*, 2008) so far. Once the surface gravity is lower than  $\log g \sim 1$ , the box-in-a-star simulations become inadequate because of the influence of sphericity becomes important; the star-in-a-box global simulations are then needed, but those are highly computer-time demanding and difficult to run, which is the reason why there are only very few simulations available so far.

RHD simulations employ realistic input physics: (i) updated and reliable equation of state, which characterize the thermodynamic state of the matter; (ii) the radiative transfer includes the most recent continuous absorption coefficients as well as atomic and molecular line opacities. The abundances employed in the computation of the simulation are the latest chemical composition by Ashland *et al.* (2009).

In particular, the radiation transport used in RHD simulations is a crucial ingredient either for the resulting atmospheric stratification and the time needed for the computation. It cannot be computed monochromatically for all the wavelength across the spectrum because of the very large computational time needed. Therefore The frequency dependance of the radiation field can be calculated with two approaches:

- the gray approximation, which completely ignores the frequency dependence, is justified only in the stellar interior and it is inaccurate in the optically thin layers. This method is often used for *star-in-a-box* simulations.
- the more elaborate scheme accounting for non-gray effects, which is based on the idea of *opacity binning* (Nordlund, 1982; Nordlund *et al.*, 1990). The basic approximation is the so called multi-group scheme (Ludwig *et al.*, 1994; Vögler *et al.* 2004). In this scheme, the frequencies that reach monochromatic optical depth unity within a certain depth range of the model atmosphere will be put into one frequency group. Actual RHD simulations use up to 5 and 12 bins (*star-in-a-box* and *box-in-a-star* simulations, respectively) to reproduce the whole frequency dependence across the full spectrum

### 3 Detailed radiative transfer to extract observables

The extraction of reliable observables require detailed monochromatic calculations. To overcome the small number of bins in RHD simulations, Chiavassa *et al.* (2009) developed a 3D pure-LTE radiative transfer code called OPTIM3D that make computation between 1000 to 200000 Å, with any spectral resolution. The code takes into account the Doppler shifts caused by convective motions. The radiative transfer equation is solved monochromatically using extinction coefficients pre-tabulated as a function of temperature, density, and wavelength (Fig. 1, left panel). The lookup tables are computed for any kind of chemical compositions using the same extensive atomic and molecular opacity data as the latest generation of MARCS models (Gustafsson *et al.*, 2008). OPTIM3D assumes a zero micro-turbulence (i.e., microscale, smaller than the free photon path, non-thermal

#### 4 What can the highest angular resolution bring to stellar astrophysics?

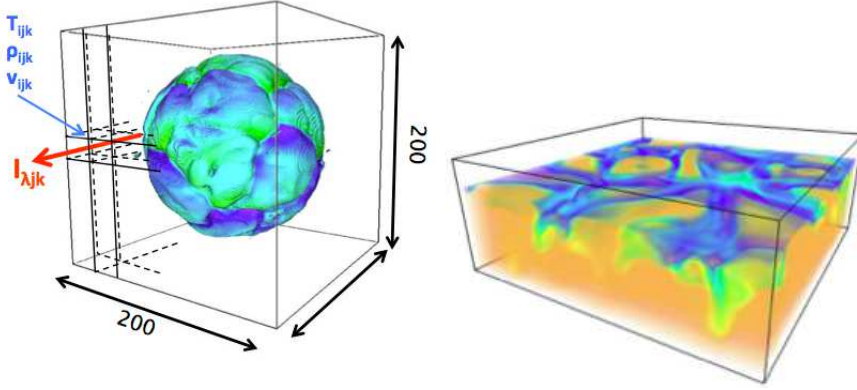


**Fig. 1.** *Left panel:* Scheme of the interaction between OPTIM3D and RHD simulations. The RHD simulation (in the *star-in-a-box* configuration, green to blue star in the middle of the numerical cube) thermodynamical variables (temperature,  $T_{ijk}$ ; density,  $\rho_{ijk}$ ; and velocity,  $v_{ijk}$ ) are used in OPTIM3D to compute the monochromatic emerging intensity ( $I_{\lambda jk}$ ) along different casting rays. *Right panel:* RHD simulation in the *box-in-a-star* configuration.

component of the gas velocity in the region of spectral line formation.) because the velocity fields inherent in RHD simulations are expected to self-consistently and adequately account for non-thermal Doppler broadening of spectral lines.

The synergy between RHD simulations and OPTIM3D allows to tackle several astrophysical problems and is based on the systematic production of observables like: high and low resolution spectra to study the chemical abundances, velocity field, and pulsations of stars as well as their stellar parameters; interferometric observables to study the stellar dynamics, stellar parameters, planet transit; and images to study the impact of convection on astrometric measurements.

#### 4 Higher spatial frequencies for the stellar granulation signal

The size of the convective cells is linked to the pressure scale height at optical-depth unity (Freytag *et al.*, 2001). The pressure scale height is defined as

$$\mathcal{H}_p = \frac{k_B T_{\text{eff}}}{mg}, \quad (4.1)$$

where  $g$  is the surface gravity,  $k_B$  is the Boltzmann constant and  $m$  is the mean molecular mass ( $m = 1.31 \times m_H = 1.31 \times 1.67 \times 10^{-24}$  grams, for temperatures lower than 10000 K). In the above expression,  $\mathcal{H}_p$  has the dimension of length. Stars with low surface gravity have more diluted atmosphere and lower surface temperature while more compact objects are hotter. Fig. 2 show the synthetic

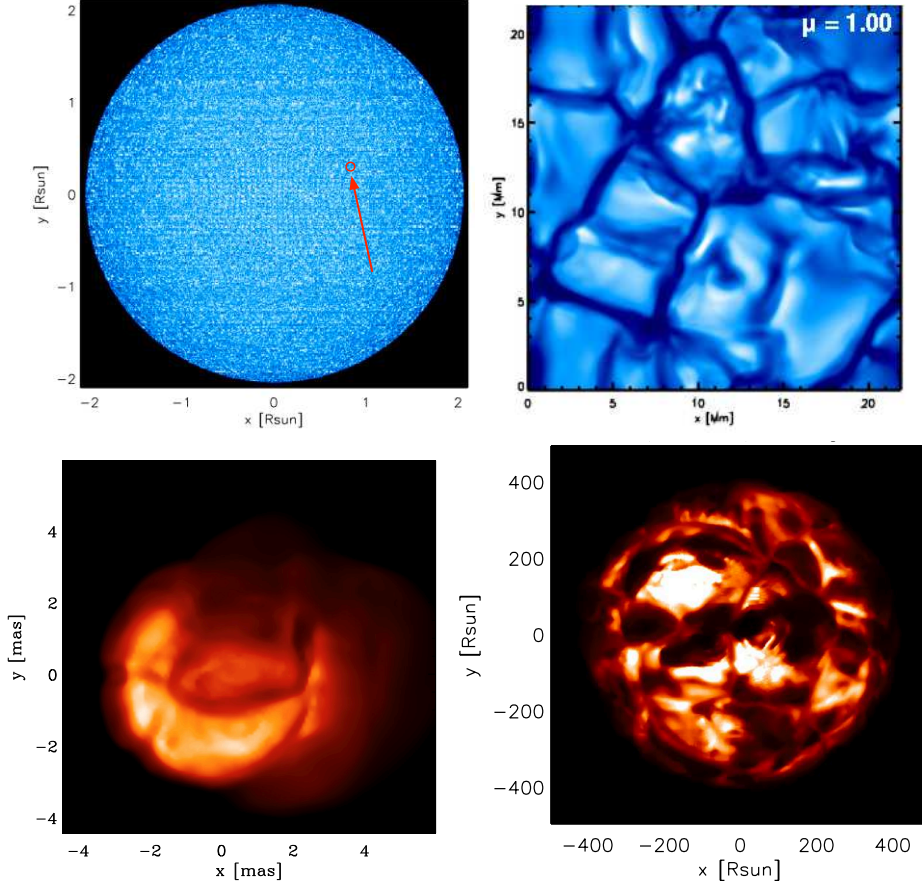


**Fig. 2.** Synthetic images of different stars computed with OPTIM3D at different wavelength and from RHD simulations. *Top left panel:* Procyon with  $T_{\text{eff}} = 6591 \pm 43$  K,  $\log g = 4.01 \pm 0.03$ , radius  $R = 2.023 \pm 0.026 R_{\odot}$ , and mass (Chiavassa *et al.*, 2012). The red circle and arrow indicate a particular zone used for the enlargement; *Top right panel:* enlargement of the surface of Procyon. *Bottom left panel:* AGB star with  $T_{\text{eff}} = 2542 \pm 220$  K,  $\log g = -0.83 \pm 0.10$ ,  $R = 443.5 \pm 58.3 R_{\odot}$ , and  $M = 1 M_{\odot}$  (Freytag *et al.*, 2008; Chiavassa *et al.*, 2010a). *Bottom right panel:* RSG star with  $T_{\text{eff}} = 3710 \pm 20$  K,  $\log g = 0.047 \pm 0.001$ ,  $R = 376.7 \pm 0.5 R_{\odot}$ , and  $M = 6 M_{\odot}$  (Chiavassa *et al.*, 2011b).

images of stars with different stellar parameters and thus different granulation pattern.

Samadi *et al.* (2013), Svensson & Ludwig (2005) and Chiavassa *et al.* (2011a) reported a direct correlation between the size of the convective cells and the stellar parameters: larger granules have larger effects on the emerging stellar flux. Following this principle, the role of long-baseline interferometric observations is to

investigate the dynamics of granulation as a function of stellar parameters: thanks to the higher angular resolution, interferometry is the ideal tool for exploring stellar convection in term of cell's size, intensity contrast and temporal variations.

#### 4.1 Evolved stars

Evolved stars, such as RSGs and AGBs, are prime targets for interferometry, because of their large diameter, proximity, and high infrared luminosity. These stars have effective temperatures lower than  $\sim 4000$  K and surface gravity lower than  $\log g = 1.0$ . Their atmospheres, resulting from the RHD simulations, is undoubtedly irregular, permeated with structures and dynamics, but depend on the wavelength probed (Fig. 2 and Fig. 3). Moreover, the surface inhomogeneities and their temporal evolution induce strong fluctuations on the intensity profiles. Fig. 4 displays the comparison between a three-dimensional image representation of the intensity in a snapshot of a RSG simulation in the H band with an ad-hoc limb-darkened image representation for a RSG star and an uniform disk. The difference is striking and the resulting RHD surface pattern full of numerous intensity spikes. These, though related to the underlying granulation pattern (characterized by very large convective cells), are also connected to dynamical effects. The emerging intensity depends on (i) the opacity run through the atmosphere (and for  $T_{\text{eff}} < 4000$  K, molecules produce strong absorption in particular in the visible) and on (ii) the shocks and waves that dominate at optical depths smaller than  $\sim 1$ .

To search for the effect of the granulation pattern on interferometric visibility curves and phases, we use the intensity maps computed with OPTIM3D (e.g., Fig. 2) and calculated a discrete Fourier transform ( $FT$ ). We introduced also a theoretical spatial frequency scale expressed in units of inverse solar radii ( $R_{\odot}^{-1}$ ). The conversion between spatial frequencies expressed in the latter scale and in the more usual scale of  $1''$  is given by:

$$\nu \left[ \frac{1}{''} \right] = \nu \left[ \frac{1}{R_{\odot}^{-1}} \right] \cdot d \text{ [pc]} \cdot 214.9 \quad (4.2)$$

where  $\nu$  is the spatial frequency, 214.9 is the astronomical unit expressed in solar radii, and  $d$  is the distance of the observed star. Also useful is the following relation

$$\nu = \frac{B}{\lambda \cdot 0.206265} \quad (4.3)$$

where  $\nu$  is the spatial frequency in  $\text{arcsec}^{-1}$  at the observed wavelength  $\lambda$  in  $\mu\text{m}$  for the baseline  $B$  of an interferometer in meters.

Fig. 5 (bottom panels) shows the visibility curves computed for 36 different angles from the intensity map of top panel. Since we do not know the exact position of the simulated star with respect to the observations, we applied a statistical approach and rotated of  $5^\circ$  the intensity map before computing the  $FT$ . Small dispersion of the visibility curves (grey thin line) around the uniform and limb-darkened disks are noticeable: the measure of the stellar diameter with uniform

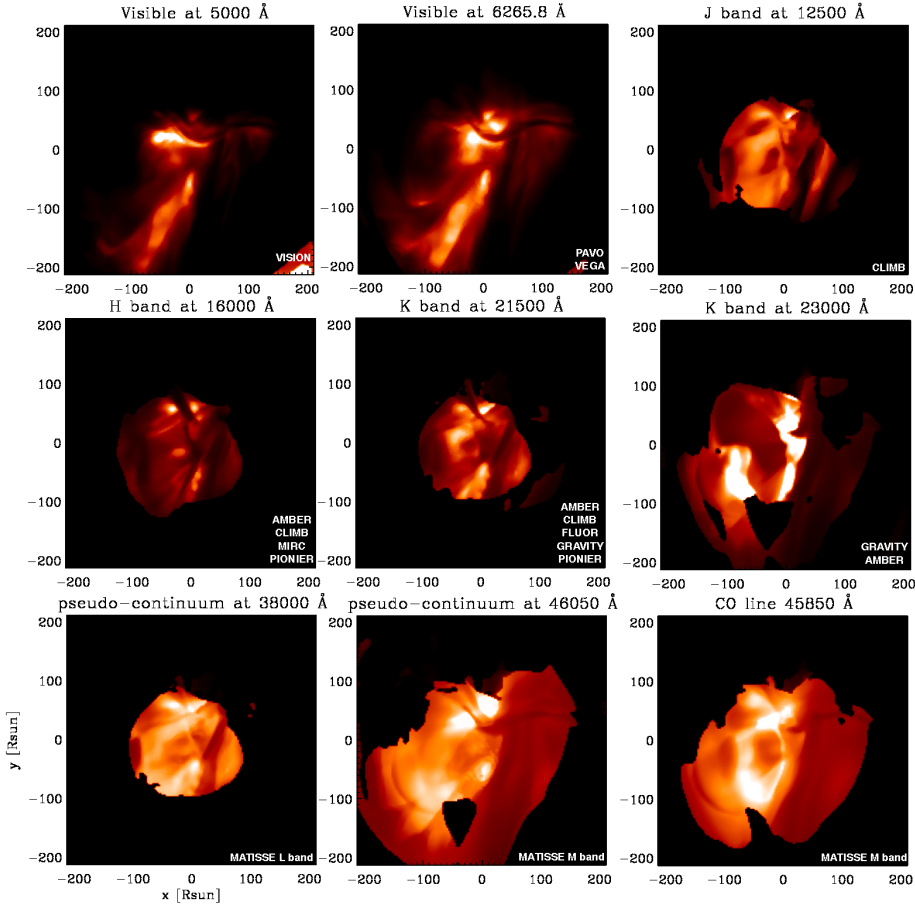


**Fig. 3.** Appearance of the stellar surface of an AGB simulation (image from Chiavassa and Freytag, 2014b) with respect to the wavelength. The present and future interferometric instrument probing these wavelengths are indicated in lower right corner of every image.

and limb-darkened disk models should take into account this dispersion as an additional uncertainty which may be up to 5% at the first null point: for example, the uniform disk spans value between 794 and 845  $R_{\odot}$  for the snapshot in Fig. 5 (bottom left panel) in order to fit the minimum and maximum amplitude of visibility fluctuations (Chiavassa *et al.*, 2009).

Moreover, the visibility dispersion increases clearly with spatial frequency (bottom right panel), and visibilities strongly deviate from the parametric cases. It is possible to characterize the typical size distribution of convective cells on RSGs using interferometric observables. Chiavassa *et al.* (2010b) used alpha Ori (RSG star) observations in H band to tackle this problem and using the following method: after

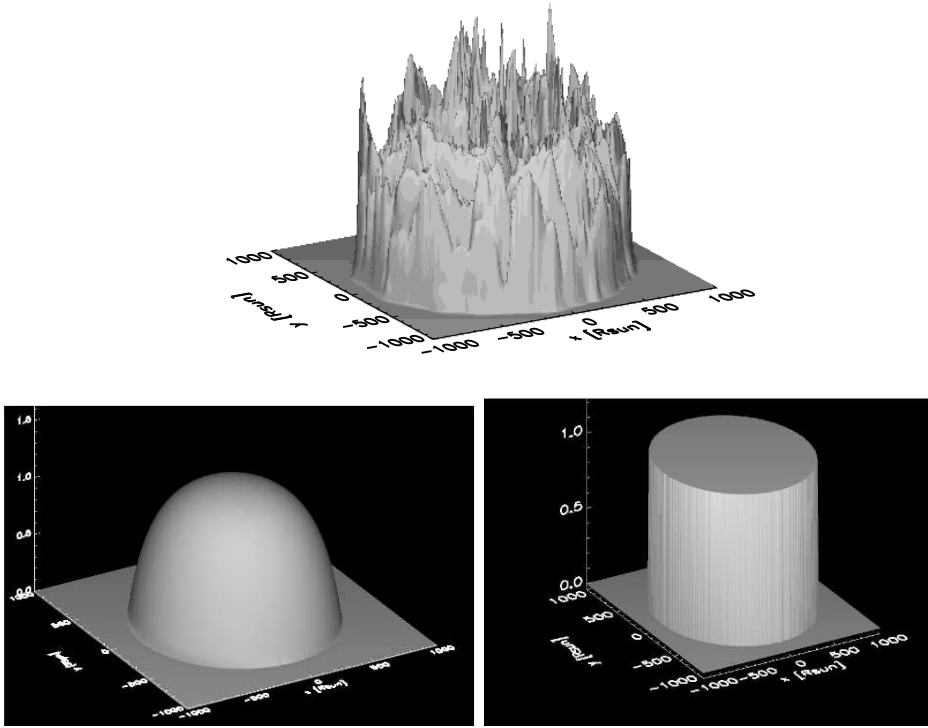


**Fig. 4.** *Top panel:* three-dimensional image of the emerging intensity from a RHD simulation of RSG star in the H band (image from Chiavassa *et al.*, 2009). *Bottom left panel:* from a limb-darkened disk with the stellar parameter of the RHD simulation. *Bottom right panel:* from a uniform disk.

the computation of the Fourier transform,  $FT$ , we obtained  $\hat{I}(u, v) = FT[I(x, y)]$ , where  $I(u, v)$  is a map like in Fig. 5. The resulting complex number  $\hat{I}(u, v)$  was multiplied by low-pass and high-pass filters to extract the information from different spatial frequency ranges (corresponding to the visibility lobes). Finally, an inverse Fourier transform,  $\bar{FT}$ , was used to obtain the filtered image:  $I_{\text{filtered}}(x, y) = \bar{FT}[\hat{I}(u, v) \cdot \text{filter}]$ .

Figure 6 (top left panel) shows the filtered images at spatial frequencies,  $\nu$ , corresponding to the first lobe of Fig. 5. Since we filtered the signal at high spatial frequencies, the image appears blurry and seems to contain only information about the stellar radius. However, the top right panel displays the signal related to all the frequencies higher than the first lobe: in this image, we clearly do not detect the central convective cell of  $\approx 30$  mas size (60% of the stellar radius, the size of



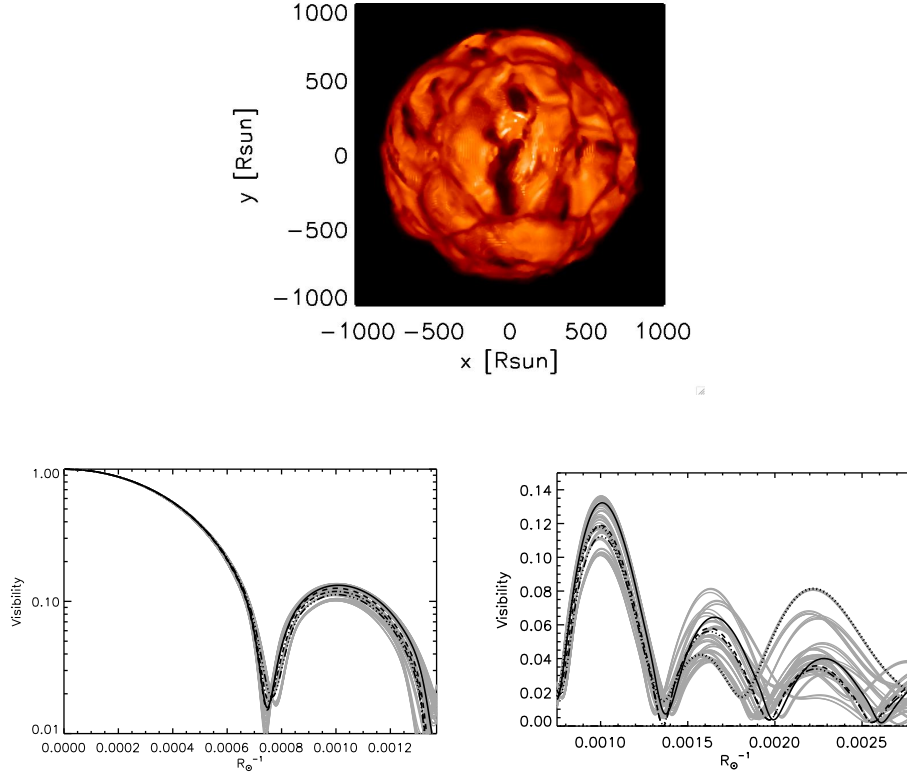


**Fig. 5.** *Top panel:* intensity maps of a RSG star in the H band. *Bottom left panel:* visibility curves (grey thin line) computed for 36 different angles with a step of  $5^\circ$  a logarithm scale is applied. The solid black curve is a uniform disk model, with a radius of  $810 R_\odot$ . The dashed black line is a partially limb-darkened disk ( $I(\mu) = 1 - 0.5(1 - \mu)$ ) with a radius of  $822 R_\odot$ . The dotted dashed line is a fully limb-darkened ( $I(\mu) = 1 - 1(1 - \mu)$ ) with a radius of  $830 R_\odot$ . The stellar parameters of this snapshot are:  $L = 98400 L_\odot$ ,  $R = 836.5 R_\odot$ ,  $T = 3534$  K and  $\log(g) = -0.34$ . Images from Chiavassa *et al.*, 2009.

alpha Ori is about 45 mas at this wavelength). Thus, the first lobe also carries information about the presence of large convective cells. Figure 6 (bottom row) shows the second lobe with convection-related structures of  $\approx 10$ -15 mas, (30% of the stellar radius), and the third and fourth lobes with structures smaller than 10 mas. We can detect convection-related structures of different size using visibility measurements at the appropriate spatial frequencies.

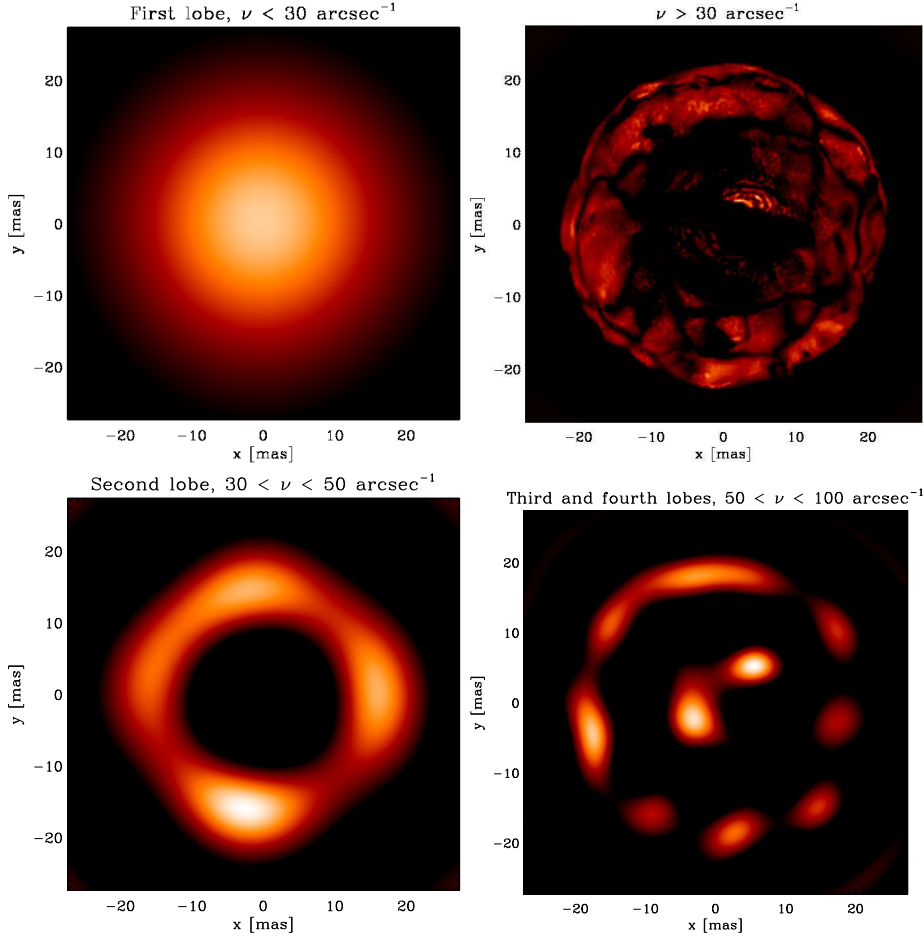


**Fig. 6.** Intensity maps filtered at different spatial frequencies qualitatively corresponding to the lobes of the visibility curve shown in Fig. 5. The size of alpha Ori is about 45 mas at these wavelengths (H band). Images from Chiavassa *et al.* (2010b).

One last important interferometric observable is the closure phase. The closure phase is defined as the phase of the triple product (or bispectrum) of the complex visibilities on three baselines, which form a closed loop joining (at least) three stations A, B, and C. If the projection of the baseline AB is  $(u_1, v_1)$ , that for BC is  $(u_2, v_2)$ , and thus  $(u_1 + u_2, v_1 + v_2)$  for AC, the closure phase is:

$$\phi_C(u_1, v_1, u_2, v_2) = \arg(V(u_1, v_1) \times V(u_2, v_2) \times V^*(u_1 + u_2, v_1 + v_2)).$$

this procedure removes the atmospheric contribution, leaving the phase information of the object visibility unaltered (Monnier, 2007 and 2003). Closure phases

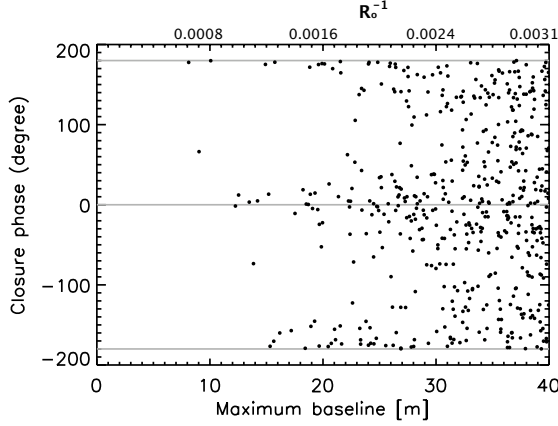


**Fig. 7.** Scatter plot of closure phases in the H band (from the intensity map of top panel of Fig. 5) of 500 random baseline triangles with a maximum linear extension of 40 m. Closure phases are plotted against the longest baseline of the triangle. The upper x-axis corresponds to synthetic observations of a RSG simulation at an apparent diameter of 43.6 mas (which corresponds to  $\alpha$  Ori at a distance of 174.3 pc). The axisymmetric case is represented by the grey lines. Image from Chiavassa *et al.*, 2009.

have the main advantage of being uncorrupted by telescope-specific phase errors, including pointing errors, atmospheric piston, and longitudinal dispersion due to air and water vapor (Le Bouquin *et al.*, 2012). Eventually, the information carried by the closure phases is intrinsically correlated with the morphology of the stellar surface inhomogeneities but depend on the relative orientation of interferometric baselines and on the distribution of the telescope station of the diluted aperture of an interferometer.

Figure 7 shows the scatter plot of the closure phase for a RHD simulation of a RSG in the H band. The closure phases deviate from zero or  $\pm\pi$  (typical values for centrosymmetric objects) already at  $\sim 10$  m ( $0.0008 R_{\odot}^{-1}$ , scaling the simulation to an apparent diameter of 43.6 mas). At higher baselines, it clearly differs from zero or  $\pm\pi$ , values that are indicating of a point symmetric brightness distribution. This is a clear signature of surface inhomogeneities. The characteristic size distribution on the stellar surface can also be derived from the closure phase: the contribution of small-scale convection-related surface structures increases with frequency. It may be very efficient to constrain the level of asymmetry of RSG atmospheres by accumulating statistics on closure phase at short and long baselines, since they are easily measured to high precision. A small departure from zero immediately enters a departure from symmetry (Chiavassa *et al.*, 2009).

RHD simulations are necessary for a proper quantitative analysis of interferometric observations of the surface of evolved stars beyond the smooth, symmetrical, limb-darkened intensity profiles. Frequencies corresponding to the first lobe (ie., sensitive to the radius) are characterized by fluctuations as high as 5%, and radii

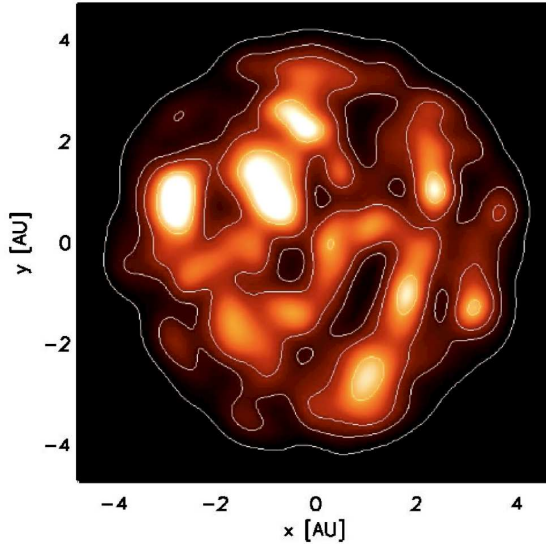


**Fig. 8.** Snapshot of a RSG simulation convolved to the PSF of a 42 m telescope approximately like the European Extremely Large Telescope (for a star at a distance of 152.4 pc). Image from Chiavassa *et al.*, 2011a.

determinations can be affected to that extent. The second, third, fourth lobes, and so on carry the signature of limb-darkening, and of smaller scale structures due the granulation, and are very different from the simple parametric cases. Also closure phases largely differ from 0 and  $\pm\pi$  with an increase of the signal with frequency, this is due to the departure from circular symmetry. The characteristic size of the granulation pattern of, eg., RSGs is composed of convection-related structures of different sizes, including small to medium scale granules (5–15 mas) and a large convective cell ( $\approx 30$  mas).

In the last years, RHD simulations managed to explain several interferometric observations of RSGs (Chiavassa *et al.*, 2009, 2010b) and AGBs (Chiavassa *et al.*, 2010a) from the visible to the infrared region. However, the final consistency check will be an image reconstruction to directly compare the granulation size and shape and the intensity contrast, provided by the planned second generation recombiner of the VLTI (MATISSE, GRAVITY, see other contributions in this book) and CHARA optical interferometry arrays. First steps in this direction has been carried out in Berger *et al.* (2012) and Malbet *et al.* (2010) where the image reconstruction algorithms have been tested using intensity maps from these RHD simulations. The European Extremely Large Telescope (E-ELT, planned to be operating in 2025) with a mirror size five times larger than a single VLT Unit Telescope will be capable of near IR observations of surface details on RSGs (Fig. 8).

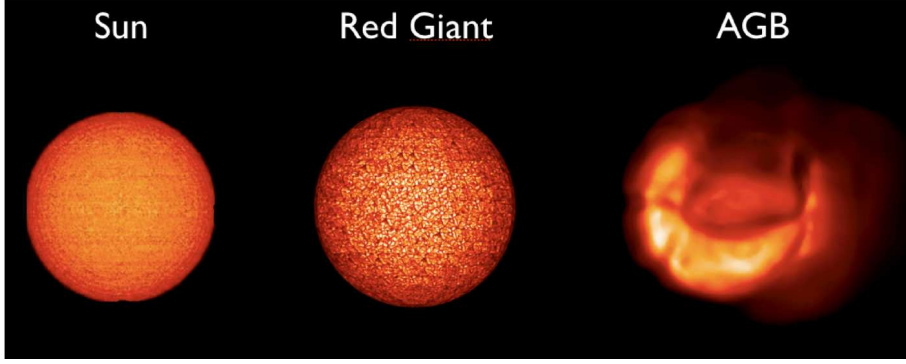


**Fig. 9.** Evolution of the surface inhomogeneities during the stellar evolution: main sequence (*left panel*), red giant (*central panel*), and AGB (*right panel*) (the scale is not preserved).

## 5 Transition from main sequence stars to evolved stars

The surface inhomogeneities at the surface of the star, i.e. the granulation aspect, depend on the effective temperature and even more important the surface gravity. The size of the granule is controlled by the stratification and the exponential drop of density at the stellar surface (e.g. Nordlund *et al.* 1990 and Stein *et al.* 1998). The effective temperature and metallicity play a less important role (Magic and Asplund 2014). On the Sun, the average granule size is about 1-2 Mm, therefore there is at least  $10^7$  granules on the entire surface. The consequence is that even if the granule aspect is very irregular, their tiny size with respect to the stellar radius makes the appearance of the surface homogenous (Fig. 9). During the evolution of a solar-type star, the radius increases by more than an order of magnitude which lowers the surface gravity, e.g.  $\log g \sim 2$  for the red giant phase and even lower than 0 for the AGB phase. The star inflates but at the same time the granule size increases to by a factor of  $10^3$  (Magic and Asplund 2014). The number of granules covering the entire surface for a red giant is much smaller than on the main sequence phase, with roughly a few thousand : the stellar surface appears more and more irregular as the star evolves.

Clearly, for the latest stage of the stellar evolution the surface of the star is very inhomogeneous. The operation of computing many Fourier transform (FT) is however costly from the numerical point of view. In the process of deriving the angular diameter of the star, one needs to compute many times the visibilities of the fringes using for example Monte Carlo procedure to derive reliable diameter and its error bars. Most of the objects for which we need precise angular diame-

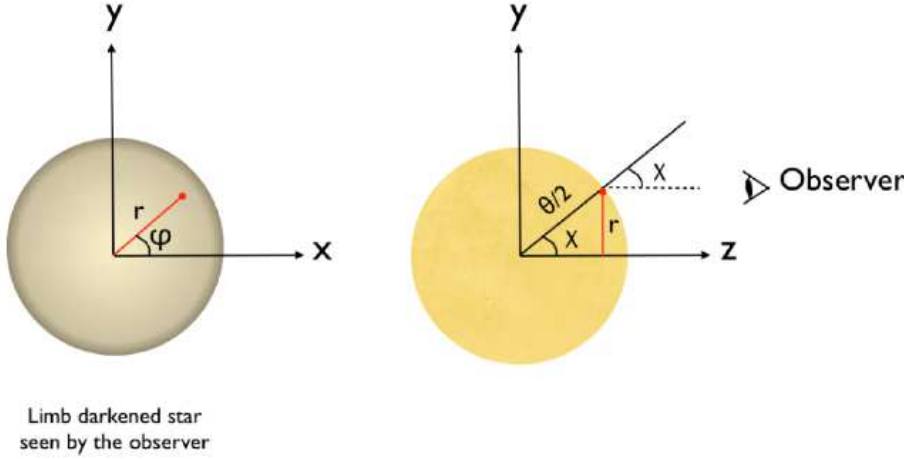


**Fig. 10.** *Left panel:* Geometry of the system. the star with axial symmetry is represented. The surface brightness depends on the position on the stellar disk,  $r$ , because of the limb darkening, but does not depend on  $\varphi$  as long as the granules are very small compared with the radius. *Right panel:* Cut of the star in the plane perpendicular to the left panel. The  $\chi$  angle measures the position on the stellar disk

ters are main sequence stars or early phase of red giants for which we can combine asteroseismology and interferometric determination of the diameter to tidily constrain the other stellar parameters (e.g., Creevey this book; Bigot *et al.* 2011 and 2015). In these cases we can take advantage of the relatively homogenous surface. The idea is to simplify the FT using axial symmetry of the star. The steps are described below.

The usual visibility in the  $(u, v)$ -plane can be computed using the theorem van Citter-Zernike (e.g., Born and Wolf 1999)

$$F(u, v) = FT[I(x, y)] = \int I(x, y) e^{2\pi i(x \cdot u + y \cdot v)} dx dy. \quad (5.1)$$

This 2D Fourier transform can be written in polar coordinates  $(r, \theta)$  where  $r$  is the position of the stellar disk  $\theta$  the azimuthal angle. Therefore  $x = r \cos \varphi$  and  $y = r \sin \varphi$  and the surface element can be transformed as  $dx dy = r dr d\varphi$  ( $r$  being the Jacobian of the transformation). The Fourier transforms writes

$$F(u, v) = \int I(r, \varphi) e^{2\pi i r(u \cos \varphi + v \sin \varphi)} r dr d\varphi. \quad (5.2)$$

It is convenient to write the coordinate  $(u, v)$  also in polar coordinates  $(k, \phi)$ . Let us, therefore define the following  $u = k \cos \phi$  and  $v = k \sin \phi$ . The Fourier transform then writes

$$F(k, \phi) = \int I(r, \varphi) e^{2\pi i r k (\cos \phi \cos \varphi + \sin \phi \sin \varphi)} r dr d\theta = \int I(r, \varphi) e^{2\pi i r k \cos(\varphi - \phi)} r dr d\varphi. \quad (5.3)$$

It is important to note that no assumption is made to derive Eq. 5.3. If the intensity is now axisymmetric then  $I(r, \varphi) = I(r)$  and we can separate the radial and angular integration. The latter is identical to a zeroth-order Bessel function of the first kind (Abramowitz and Stegun 1972).

$$\int e^{i k r \cos(\varphi - \phi)} d\theta = 2\pi J_0(kr). \quad (5.4)$$

In the latter expression, the  $\phi$  coordinate disappeared since for any value of  $\phi$  we can always make a change of variable so that  $\int e^{2\pi i k r \cos(\varphi - \phi)} d\varphi = \int e^{2\pi i k r \cos(\varphi')} d\varphi'$ . The Fourier transform of the stellar disk intensity in the case of axial symmetry simplifies to a 1D integral

$$F(k) = 2\pi \int_0^{\theta/2} I(r) J_0(kr) r dr, \quad (5.5)$$

which is the Hankel transform of the disk intensity  $I(r)$ . Since  $k$  is the spatial frequency we have  $k = B/\lambda$ , where  $B$  is the baseline between the two telescopes and  $\lambda$  is the wavelength of the measurement. The position,  $r$ , on the stellar disk measures the distance between the disk center  $r = 0$  and the limb  $r = \theta/2$ , where  $\theta$  is the angular diameter of the star. It is common to express since distance in term of the angle  $\chi$  made by the vertical (disk center) and the line-of-sight of an observer (see Fig. 10). Therefore the position of the stellar disk is simply  $r = \theta/2\sqrt{1 - \mu^2}$  and  $dr/r = -1/(1 - \mu^2)\mu d\mu$  where  $\mu = \cos \chi$ .

With these definition we can rewrite the visibilities as

$$V \propto \int_0^1 I(\mu) J_0(\pi \sqrt{1 - \mu^2} \theta B/\lambda) \mu d\mu \quad (5.6)$$

which is the usual expression using for fitting angular diameters from the computed limb-darkened intensities.

### 5.1 Main sequence and giant stars

As explained in Section 2, the computational domain of RHD simulations of main sequence and K giant stars represents only a small portion of the stellar surface. To overcome this limitation, and at the same time account for limb-darkening effects, Chiavassa *et al.* (2010c, 2012, 2014a) computed intensity maps for different inclinations ( $\theta$ -angles) with respect to the vertical direction and for representative series (covering several convection turnover) of simulation snapshots and used them to tile a spherical surface. The computed values of the  $\theta$ -angle depend on the position (longitude and latitude) of the tile on the sphere and are linearly interpolated among the inclination angles. In addition to this, the statistical tile-to-tile

fluctuations (i.e., number of granules, shape, and size) is taken in consideration by selecting random snapshots within each simulation's time-series. As a consequence, the simulation assumption of periodic boundary conditions resulted in a tiled spherical surface globally displaying an artifactual periodic granulation pattern. However, the resulting artificial signal introduced in the interferometric observables is less important than the one caused by the inhomogeneities of the stellar surface. The final result is an orthographic projection (i.e., stellar disk image as seen from a nearby observer) of the tiled spheres (Fig. 2 and 11).

The extraction of interferometric observables is done using the stellar disk images and the *FT* method described in the previous sections. However, only closure phases are sensitive enough to the effect of stellar granulation to expect a possible detection with today interferometers. Chiavassa *et al.* (2014a) computed the closure phases for twelve interferometric instruments covering wavelengths ranging from visible to infrared, optimizing the observability to allow a broad coverage of spatial frequencies. The aim of that work is to present a survey of the granulation pattern of stars with different stellar parameters and to evaluate its effect on the detection of planet transit. Fig. 11 displays inhomogeneous brightness distributions in the disk images; moreover, the centre-to-limb variations are more pronounced in the visible instruments with respect to the infrared ones. This effect is explained by different sensitivity of the source (Planck) function at visible and at infrared wavelengths.

Figure 13 (top panel) displays one example from Chiavassa *et al.* (2014a) of closure phases deviating from the axisymmetric case for MIRC-6 telescope configuration case. The scatter plot of closure phase increase particularly in the visible wavelength range, where the dispersion is larger (e.g., VEGA, NPOI, and PAVO instruments). Depending on the instruments and spatial frequency spanned, the departures from symmetry may be large or not. However, it is apparent that the convection-related surface structures have a signature on the closure phases.

Figure 13 (bottom panel) shows indeed a direct application to two real targets: Beta Com, G0V star with angular diameter of 1.1 mas (Richichi *et al.*, 2005); and Procyon, F5IV with angular diameter of 5.4 mas (Chiavassa *et al.*, 2012). In general, all the instruments (except for MATISSE and NPOI, which do not probe frequencies larger than the first lobe) show closure phases departures ( $\psi$ ) of the order of few degrees with largest values of the order of  $\sim 16^\circ$ . These values are much larger than what are the actual instrument's uncertainties. More in detail:

- PAVO and VEGA show departures lower than  $0.5^\circ$  already on the 2nd lobe (VEGA instrument);
- AMBER and GRAVITY with values lower than  $0.8^\circ$ ;
- PIONIER in the H band with values of  $4.3^\circ$  (2nd lobe)  $6.4^\circ$  (3rd lobe), and PIONIER in the K band with  $2.9^\circ$  (2nd lobe);
- MIRC with  $13.8^\circ$ ,  $15.3^\circ$ ,  $16.4^\circ$ ,  $13.1^\circ$  for the 3rd, 4th, 5th, 6th lobe, respectively;





**Fig. 11.** Synthetic stellar disk images of different RHD simulations (columns). The images correspond to a representative wavelength for each interferometric instruments from the visible (top row) to the far infrared (bottom row). The averaged intensity ( $\times 10^5 \text{ erg cm}^{-2} \text{ s}^{-1} \text{ Å}^{-1}$ ) is reported in the lower left corner of each image. Image from Chiavassa *et al.* (2014a).

- CLIMB J band with  $6.5^\circ$ ,  $0.2^\circ$ ,  $5.1^\circ$  for the 3rd, 4th, 5th lobe, respectively;
- CLIMB K band with  $12.3^\circ$ ,  $6.3^\circ$  for the 3rd, 4th lobe, respectively.

The actual instruments and telescopes allow, in principle with very good weather conditions, the detection of the granulation. The closure phase signal is already more pronounced in the infrared for the 2nd lobe and may be detected with very good weather and instrumental conditions but it is certainly easier to detect from the 3rd lobe on. MIRC instrument with 6 telescope recombination is the most appropriate instrument as it combines good UV coverage and long baselines probed.

Another important role of long-baseline interferometric observations is planet hunting as a complement to the radial velocity and adaptive optics surveys. High

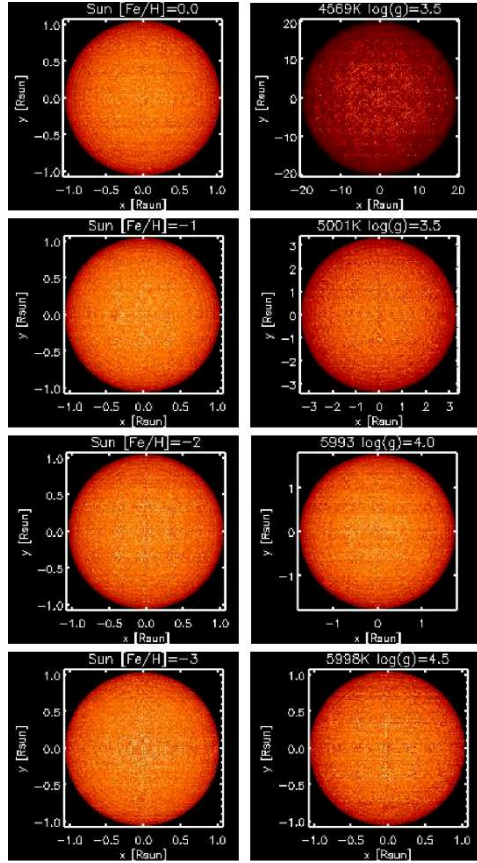


**Fig. 12.** Enlargement of the synthetic stellar disk images of Fig. 11 for the VEGA instrument mounted at CHARA interferometer. Image from Chiavassa *et al.* (2014a).

angular resolution is an ideal tool for exploring separations in the range 1 to 50 mas (Le Bouquin *et al.*, 2012). In addition to this, Chiavassa *et al.* (2014a) measured the contamination of granulation signal on the planetary transit using closure phases. To do this, the authors chose three prototypes of planets representing different sizes and compositions because the purpose is not to reproduce the exact conditions of the planet-star system already detected but to have a statistical approach on the interferometric signature for different stellar parameters hosting planets with different sizes. Then they created transiting images (Fig. 14, top) and computed the resulting closure phases. Eventually, they determined the differences between planet-star system and the star alone (Fig. 14, bottom). For all the instruments, the absolute difference scales with the size of the planet considered: the smaller planet returns smaller differences. In addition to this, the differences are larger in the visible wavelengths where the granulation contrast is higher than

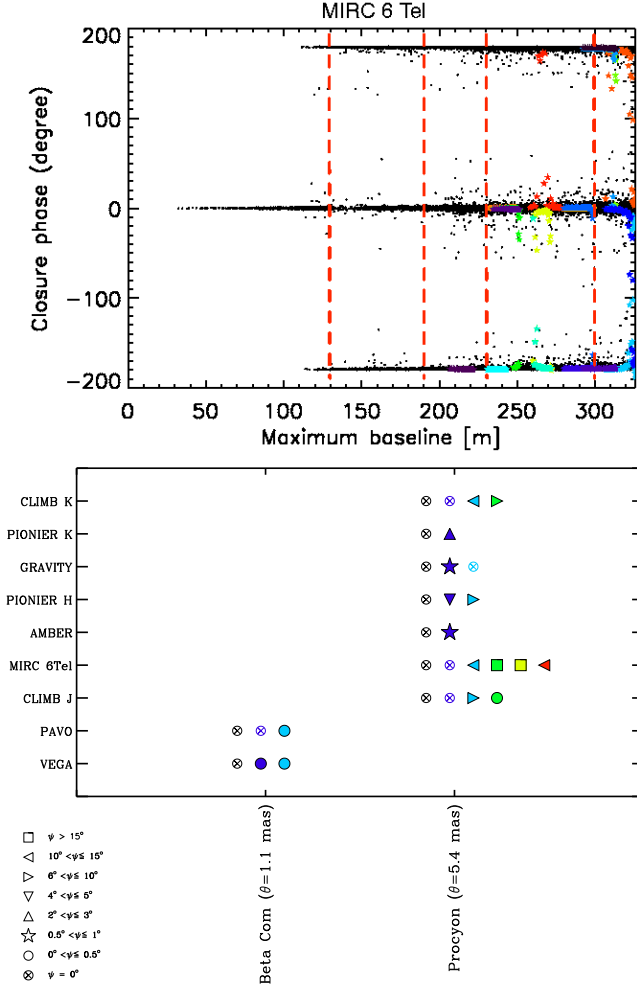


**Fig. 13.** *Top panel:* Scatter plot of closure phases of 20000 random baseline triangles (black dots) as a function of the maximum linear extension corresponding to the configuration chosen for each MIRC instrument and for the RHD simulation of the Sun. The colored symbols over-plotted display the closure phases for a particular telescope configuration chosen and the vertical dashed red lines give the approximative positions of the different lobes. *Bottom panel:* Departure,  $\psi$ , of closure phases from zero and/or  $\pm\pi$  (i.e., no axisymmetric case) for RHD simulations with stellar parameters corresponding to two real stars (horizontal axis) and different interferometric instruments (vertical axis). 6 lobes are displayed: black for the 1st lobe, violet for the 2nd, light blue for the 3rd, green for the 4th, yellow for the 5th, and red for the 6th. Only the lobes spanned in the UV-planes are plotted. The symbols correspond to different values, in degrees. Images from Chiavassa *et al.* (2014a).

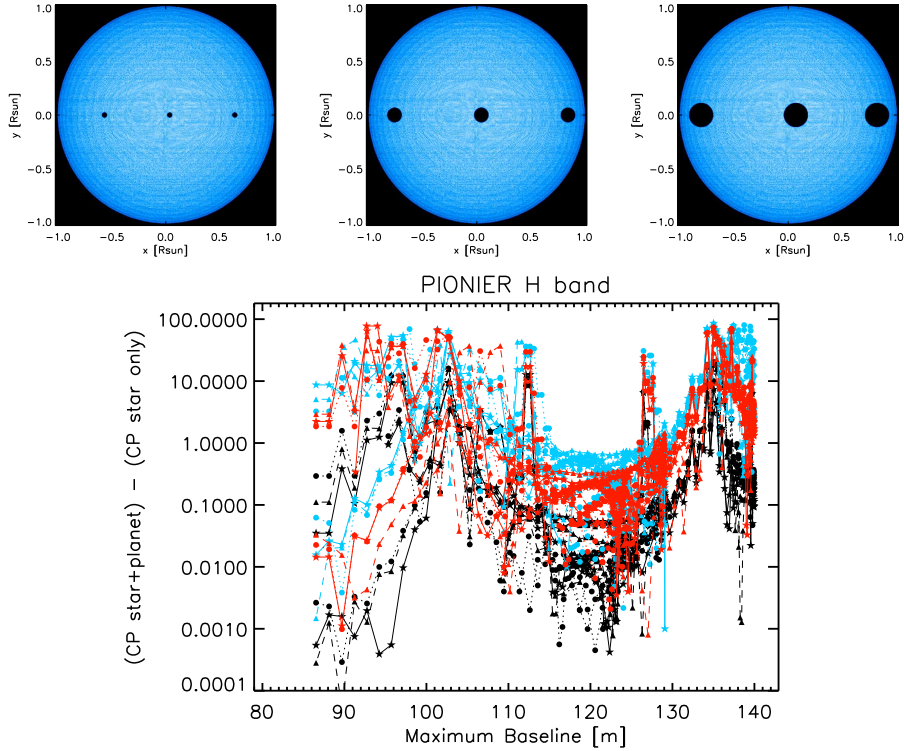


**Fig. 14.** *Top:* Synthetic stellar disk images in H band (PIONIER instrument) together with three planet transiting phases (black color) for a star like the Sun. The prototypes of planet have parameters corresponding to: Kepler-11 f (left), HD 149026 b (central), and CoRoT-14 b (right). *Bottom:* Absolute closure phase differences (in degrees) between the star with a transiting planet (from above) and the star alone (Fig. 11). The black colour correspond to Kepler 11-f, the red to HD 149026 b, and the blue CoRoT 14-b. The star symbols connected with solid lines correspond to the planet phase entering in the stellar disk, the circle symbols connected with dotted line to the planet at the centre of the stellar disk, and the triangles connected with dashed line to the planet exiting the stellar disk. Images from Chiavassa *et al.* (2014a).

in the infrared.

The signature of the transiting planet on the closure phase is mixed with the signal due to the convection-related surface structures. The time-scale of granulation depends on the stellar parameters, and varies from minutes or tens of minutes for solar type stars and sub-giants, to hours for more evolved red giant stars. If the transit is longer than the granulation time-scale (which is the case for most of main sequence stars), it is possible to disentangle its signal from convection by

observing at particular wavelengths (either in the infrared or in the visible) and measuring the closure phases for the star at difference phases of the planetary transit.

For this purpose, it is very important to have a comprehensive knowledge of the host star to detect and characterize the orbiting planet, and RHD simulations are very important to reach this aim.

## 6 Stellar parameters

Stellar parameters determined with interferometric techniques often consist into a simple uniform disk model-fitting that, although unphysical, has the advantage of immediately telling if a star is resolved, after which limb-darkening corrections are applied. Chiavassa *et al.* (2010c) reported the effect on stellar parameter determination of 3D intensity distribution with respect to 1D models. This has been carried out using synthetic intensity profiles (Fig. 15, top) from 3D simulations with different stellar parameters and metallicities that have been compared to 1D models with exactly the same parameters.

The visibility can be derived using  $V_\lambda(B, \Theta)$  from the intensity profile  $I(\lambda, \mu)$  using the Hankel integral:

$$V_\lambda(B, \Theta) = \frac{1}{A} \int_0^1 I(\lambda, \mu) J_0\left(\frac{\pi B \Theta}{\lambda} \sqrt{1 - \mu^2}\right) \mu d\mu \quad (6.1)$$

where  $\lambda$  is the wavelength in meters,  $B$  is the baseline in meters,  $\Theta$  is an arbitrary angular diameter in radians (2 mas here),  $J_0$  the zeroth order of the Bessel function,  $\mu = \cos(\theta)$  (with  $\theta$  the angle between the line of sight and the radial direction), and  $A$  the normalization factor:

$$A = \int_0^1 I(\lambda, \mu) \mu d\mu \quad (6.2)$$

For typical red giant stars having  $4600 < T_{\text{eff}} < 5100$  K, the differences in angular diameters vary from about  $-3.5\%$  to about  $1\%$  in the visible, and are roughly in the range between  $-0.5$  and  $-1.5\%$  in the infrared (Table 1), the corresponding change in effective temperature being  $\Delta T_{\text{eff}}/T_{\text{eff}} = 1 - \sqrt{\Theta_{3D}/\Theta_{1D}}$ .

While the impact of the corrections in Table 1 is usually not dramatic, they are not negligible to properly set the zero point of the effective temperature scale derived by mean of this fundamental method. In particular in the visible, the (partially) resolved (very) metal-poor stars, it is important to take those corrections into account for a correct derivation of their diameters. A second point of concern is the reliability of the existing catalogs of calibrator stars for interferometry that are based on red giants: the formal high accuracy (a fraction of  $1\%$ ) based on 1D models on diameter determination (Mérand *et al.* 2010) may be impacted by the correction reported in Table 1.

Interferometry is advantageous in that it provides the ability to directly measure stellar angular diameters and effective temperatures. However, there is a non-negligible and still partly unexplored model dependence (Casagrande *et al.*, 2014).

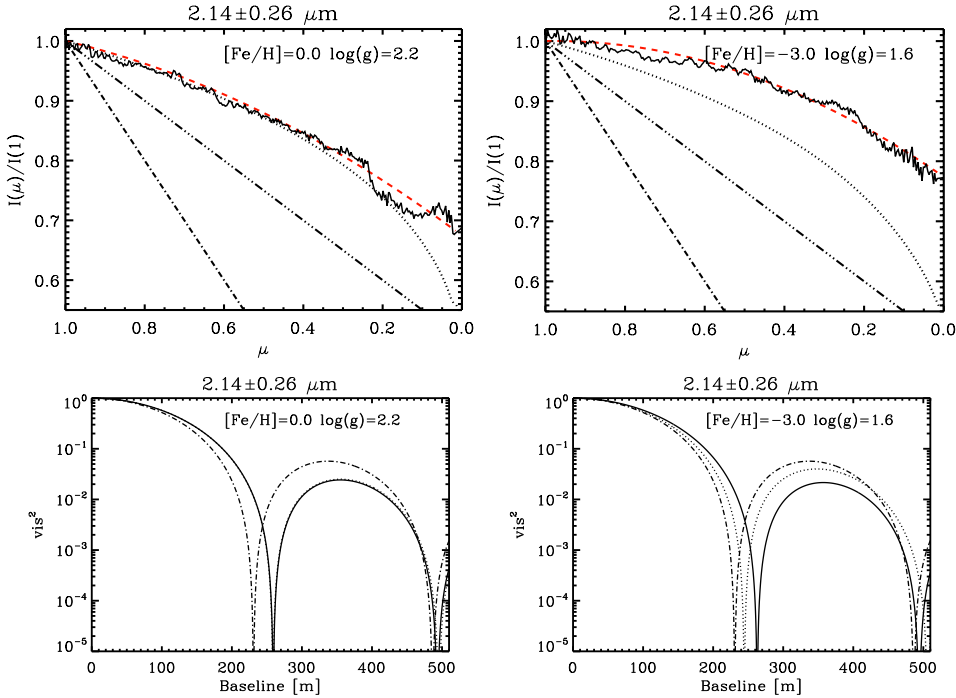


**Fig. 15.** *Top panels:* limb-darkening fits (red dashed line) for the RHD azimuthally average intensity profile (solid line) for a solar metallicity K giant star (left) and a metal poor one (right). The dotted line is the intensity profile computed with the 1D model having identical stellar parameters, input data, and chemical compositions as the 3D simulation. Parametric full (dash-dotted line) and partial limb-darkening (triple dot-dashed line) are also shown. *Bottom panels:* Visibility curves computed with Hankel transform with a fixed angular diameter of 2 mas for the above intensity profiles of the 3D simulation (solid line), 1D (dotted line), and fully limb-darkening (dash-dotted line). A logarithm scale is used on y-axis. Synthetic visibilities in these plots are not realistic near the nulls but are intended only for model-to-model comparison. Images from Chiavassa *et al.* (2010c).

More details about the link between stellar parameters, interferometry and asteroseismology are reported in Creevey’s contribution to this book.

## 7 Additional notes on chromospheric stellar activity with interferometry

The chromosphere (in the classical, stratified, and highly oversimplified view) is an intermediate region in the atmosphere of a star, lying above the photosphere and below the corona. Chromospheric activity, which encompasses diverse phenom-

**Table 1.** Ratio between the limb-darkened diameters recovered using 1D models ( $\Theta_{1D}$ ) or 3D simulations ( $\Theta_{3D}$ ) and the corresponding change in effective temperature  $\Delta T_{\text{eff}}$  for the RHD simulations. Table from Chiavassa *et al.* (2010c).

$\lambda$ [ $\mu\text{m}$ ]	[Fe/H]	$\log g$	$\Theta_{3D}/\Theta_{1D}$	$\Delta T_{\text{eff}}$ [K]
0.5 <sup>a</sup>	0.0	2.2	1.003	−7
2.14 <sup>b</sup>	0.0	2.2	0.996	9
0.5	−1.0	2.2	0.991	21
2.14	−1.0	2.2	0.996	9
0.5	−2.0	2.2	0.982	46
2.14	−2.0	2.2	0.990	25
0.5	−3.0	2.2	1.011	−28
2.14	−3.0	2.2	0.989	28
0.5	−3.0	1.6	0.965	82
2.14	−3.0	1.6	0.984	37

<sup>a</sup>central wavelength of the corresponding visible filter used in Chiavassa *et al.* (2010c)

<sup>b</sup>central wavelength of the corresponding FLUOR (K band) filter used in Chiavassa *et al.* (2010c)

ena that produce emission in excess of that expected from a radiative equilibrium atmosphere, is tightly linked to changes in the stellar magnetic field, whether periodic or irregular, and is therefore tied to the structure of the subsurface convection zone, the stars rotation, and the regeneration of the magnetic field via a self-sustaining dynamo (Hall,2008).

Activity signature may manifest in changes in the radiative transfer of lines formed very high in the atmosphere of a star, typically for spectral lines sensitive to the increase in temperature of the atmosphere. The hydrogen Balmer lines and the doublet H&K of the Ca II are used to estimate the strength of the chromospheric activity. Mg II lines in the ultraviolet can also help in this direction.

The advent of a new instruments (VEGA at CHARA), working in near IR and visible, opened the possibility to probe and characterize the chromosphere using interferometry: for this purpose H $\alpha$  and Ca II triplet lines have been observed using VEGA to extract the signature of stellar activity of a late-type K giant star (Berio *et al.*, 2011). The authors managed to determine the physical extents of the chromosphere of the star measuring the ratio of the radii of the photosphere with respect to the chromosphere using the interferometric measurements in the H $\alpha$  and the Ca II infrared triplet line cores. These interferometric measurements are unique and crucial to constrain chromospheric models.

## References

- Abramowitz, M., & Stegun, I. A. 1972, Handbook of Mathematical Functions, New York: Dover, 1972,
- Asplund, M., Grevesse, N., Sauval, A. J., & Scott, P. 2009, A&AR, 47, 481

- Berger, J.-P., Malbet, F., Baron, F., et al. 2012, A&AR, 20, 53
- Berio, P., Merle, T., Thévenin, F., et al. 2011, A&A, 535, AA59
- Bigot, L., Mourard, D., Berio, P., et al. 2011, A&A, 534, LL3
- Bigot, L. *et al.* 2015, in preparation for A&A
- Born, M., & Wolf, E. 1999, Principles of Optics, by Max Born and Emil Wolf and With contributions by A. B. Bhatia and P. C. Clemmow and D. Gabor and A. R. Stokes and A. M. Taylor and P. A. Wayman and W. L. Wilcock, pp. 986. ISBN 0521642221. Cambridge, UK: Cambridge University Press, October 1999.
- Carlsson, M., Stein, R. F., Nordlund, A&A, & Scharmer, G. B. 2004, ApJ, 610, L137
- Casagrande, L., Portinari, L., Glass, I. S., et al. 2014, MNRAS, 439, 2060
- Chiavassa, A., Plez, B., Josselin, E., & Freytag, B. 2009, A&A, 506, 1351
- Chiavassa, A., Lacour, S., Millour, F., et al. 2010a, A&A, 511, A51
- Chiavassa, A., Haubois, X., Young, J. S., et al. 2010b, A&A, 515, A12
- Chiavassa, A., Collet, R., Casagrande, L., & Asplund, M. 2010c, A&A, 524, A93
- Chiavassa, A., Pasquato, E., Jorissen, A., et al. 2011a, A&A, 528, A120
- Chiavassa, A., Freytag, B., Masseron, T., & Plez, B. 2011b, A&A, 535, A22
- Chiavassa, A., Bigot, L., Kervella, P., et al. 2012, A&A, 540, A5
- Chiavassa, A., Ligi, R., Magic, Z., et al. 2014, A&A, 567, AA115
- Chiavassa, A., & Freytag, B. 2014, arXiv:1410.3868
- Dawes, W. R. 1864, MNRAS, 24, 161
- Dravins, D. 1987, A&A, 172, 211
- Freytag, B. 2001, 11th Cambridge Workshop on Cool Stars, Stellar Systems and the Sun, 223, 785
- Freytag, B., Hoefner, S. 2008, A&A, 483, 571
- Freytag, B., Steffen, M., Ludwig, H.-G., et al. 2012, Journal of Computational Physics, 231, 919
- Gray, D. F. 2005, "The Observation and Analysis of Stellar Photospheres, 3rd Edition, by D.F. Gray. ISBN 0521851866.
- Gustafsson, B., Edvardsson, B., Eriksson, K., et al. 2008, A&A, 486, 951
- Hall, J. C. 2008, Living Reviews in Solar Physics, 5, 2
- Herschel, W. 1801, Royal Society of London Philosophical Transactions Series I, 91, 265
- Le Bouquin, J.-B., & Absil, O. 2012, A&A, 541, A89
- Ludwig, H.-G., Jordan, S., & Steffen, M. 1994, A&A, 284, 105
- Ludwig, H.-G., Caffau, E., Steffen, M., et al. 2009, Memorie della Societ Astronomica Italiana, 80, 711
- Magic, Z., Collet, R., Asplund, M., et al. 2013, A&A, 557, A26
- Magic, Z., & Asplund, M. 2014, arXiv:1405.7628
- Malbet, F., Cotton, W., Duvert, G., et al. 2010, SPIE, 7734,
- Mérand, A., Kervella, P., Barban, C., et al. 2010, A&A, 517, A64
- Monnier, J. D. 2003, Reports on Progress in Physics, 66, 789
- Monnier, J. D. 2007, New Astronomy Reviews, 51, 604
- Nordlund, A. 1982, A&A, 107, 1
- Nordlund, A., & Dravins, D. 1990, A&A, 228, 155



- Stein, R. F., & Nordlund, Å. 1998, *ApJ*, 499, 914
- Nordlund, Å., Stein, R. F., & Asplund, M. 2009, *Living Reviews in Solar Physics*, 6, 2
- Vögler, A., Bruls, J. H. M. J., & Schüssler, M. 2004, *A&A*, 421, 741
- Richichi, A., Percheron, I., & Khristoforova, M. 2005, *A&A*, 431, 773
- Samadi, R., Belkacem, K., Ludwig, H.-G., et al. 2013, *A&A*, 559, A40
- Svensson, F., & Ludwig, H.-G. 2005, 13th Cambridge Workshop on Cool Stars, Stellar Systems and the Sun, 560, 979